Numerical investigation of the flow evolution of an oscillating foil with the different reduced frequency

M J Zhang[1], Q Wu[2,1*] and B Huang[1]

1. School of Mechanical Engineering, Beijing Institute of Technology, Beijing 100081, China
2. Department of Thermal Engineering, Tsinghua University, Beijing 100084, China

E-mail: wuqin919@bit.edu.cn

Abstract. The power extraction systems based on oscillating foil are played more and more attention in alternative energy extraction systems. The dynamic stall problem on oscillating foil is related to general performance of energy extraction systems, where a varying flow filed is introduced by a rapid change in the effective angle of attack. The objective of this paper is to investigate the flow evolution of an NACA0012 foil undergoing sinusoidal pitching motion with the different reduced frequency. The k-ω SST turbulence model, coupled with a two-equation γ-Re_θ transition model, is used for the turbulence closure. The results showed that the numerical method can well capture the dynamic stall process. With the increasing of the reduced frequency, the dynamic stall is delayed during the development of the Leading Edge Vortex stage. During post-stall vortex shedding stage, the mechanism of post-stall vortex shedding present different style at different reduced frequency K. When K=0.1, the secondary vortex forms and covers the whole suction face again along with the shedding of LEV. Compared to the case of K=0.1, no secondary vortex was induced for K=0.05. However, When K=0.2, the secondary vortex covers the whole suction surface again because the oscillating velocity is too fast to develop the secondary vortex.

1. Introduction

With the high cost of non-renewable fossil fuels, the development of renewable energy sources have been promoted [1][2][3]. Among the various renewable energy, wind energy has attracted a lot of attention because it is resource-rich, widely distributed, clean. Additionally, the wind turbines that can convert the wind energy into electricity have also achieved great development [4][5][6]. Among the wind turbine system, the wind turbine blades often play an important role. However, the dynamic stall problem on the wind turbine blades is related to general performance of the wind turbine, where a varying flow filed is introduced by a rapid change in the effective angle of attack [7][8][9]. Hence, it is of significant importance to understand the dynamic interactions between the transient wing motion and unsteady flow conditions. Moreover, as one of the primary flow energy conversion technologies, an improved understanding will help the oscillating wing system to enhance the energy harvest performance for wind or hydro energy.

Many experimental and numerical investigations on aerodynamic performance of an oscillating foil have been conducted. Yang[10] utilized a videometric technique to measure the deformation of large-scale wind turbine blade in the full-scale tests and during operation. The results indicate the deformation of composite wind turbine blades would affect the performance of the wind turbine.

McKinney[11] applied a pitching wing to investigate a windmill to extract wind energy. The results presented the windmill can extract energy compared with rotary designs. LEE and Gerontakos[12] investigated the transient behaviour of the blade surface unsteady boundary layer and the characteristics of the dynamic stall events associated with an oscillating NACA0012 airfoil with multiple hot-film sensor arrays and smoke flow visualizations measurement. The results showed the unsteady flow mechanisms and the influence of the reduced frequency, oscillation amplitude on dynamic characteristics.

With the increasing of the computing resources, much attention has been paid to the computational fluid dynamics technique. Liu[13] studied the dynamic stall characteristics of an S809 airfoil undergoing translational motion as well as pitching motion with the Computational Fluid Dynamics (CFD) techniques. Simulation results indicated that both the out-of-plane and in-plane translational motions of the airfoil affect the unsteady aerodynamic forces significantly. Danao[14] investigated the effects of various rotor blade thickness and camber on the performance of a vertical axis wind turbine, where the NACA0012, NACA0022, NACA5522 and LS0421 are employed. The results showed slightly cambered foils can improve the overall performance of the vertical axis wind turbine because of generating higher values of torque in both the upwind and the downwind regions. Huang[7][15][16] numerically investigated a hydrofoil undergoing transient up-and-down pitching motion at various pitching velocities. It revealed that the flow experienced complex boundary layer events such as laminar-to-turbulence transition and the pitching velocity had a significant effect on the transition and hydrodynamic load.

Although much work has been done to investigate the dynamic performance of oscillating wings[17][18][19], the significant uncertainty of the impact of the unsteady flow features on the power generation and also energy harvest system still exists. The objective of this study is to analyze the influence of the reduced frequency on the transient vortex structures around an oscillating foil, and to further improve the understanding of the interplay between unsteady flow, oscillatory motion of the foil and the dynamic performance. The numerical models are presented in Section 2, followed by the summary of numerical set-up in Section 3. In Section 4, detailed analysis of the influence on the flow evolution is presented. Finally, the conclusions are summarized in Section 5.

2. Numerical model

2.1. Basic governing equations
The flow field of oscillating foil is simulated by solving the 2D unsteady Reynolds-averaged Navier-Stokes equations, with the continuity and momentum equation listed below:

$$\frac{\partial \rho}{\partial t} + \frac{\partial (\rho u_j)}{\partial x_j} = 0 \tag{1}$$

$$\frac{\partial (\rho u_i)}{\partial t} + \frac{\partial (\rho u_i u_j)}{\partial x_j} = -\frac{\partial p}{\partial x_i} + \frac{\partial}{\partial x_j}\left(\mu \frac{\partial u_i}{\partial x_j} \right) \tag{2}$$

where, ρ is the fluid density, t is time, u is the velocity, x is the coordinate, p is the pressure, μ is the fluid viscosity, and subscripts i and j denote the directions of the Cartesian coordinates.

2.2. Turbulence model
The current simulation solves the URANS equations using the revised k-ω SST turbulence model, which couples the k-ω SST turbulence model proposed by Menter[20] and the γ-Re_θ transition model[21][22][23].
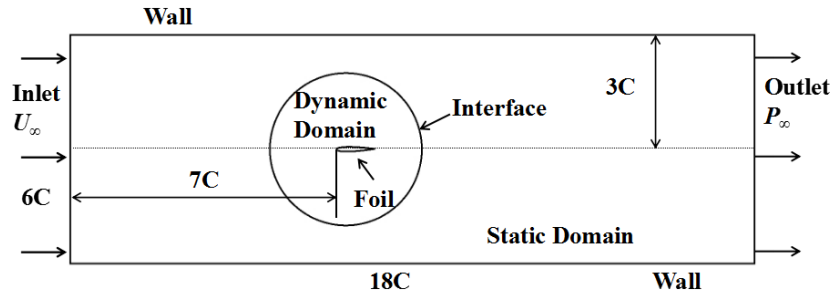
$$\frac{\partial (\rho k)}{\partial t} + \frac{\partial (\rho u_j k)}{\partial x_j} = \tilde{P}_k - \tilde{D}_k + \frac{\partial}{\partial x_j}\left[(\mu + \sigma_k \mu_t) \frac{\partial k}{\partial x_j} \right] \tag{3}$$

$$\frac{\partial(\rho\omega)}{\partial t}+\frac{\partial(\rho U_j\omega)}{\partial x_j}=C_\omega P_\omega-\beta_\omega\rho\omega^2+\frac{\partial}{\partial x_i}\left[\left(\mu+\frac{\mu_t}{\sigma_k}\right)\frac{\partial\omega}{\partial x_i}\right]+2\rho(1-F_1)\sigma_{\omega2}\frac{1}{\omega}\frac{\partial k}{\partial x_i}\frac{\partial\omega}{\partial x_i} \quad (4)$$

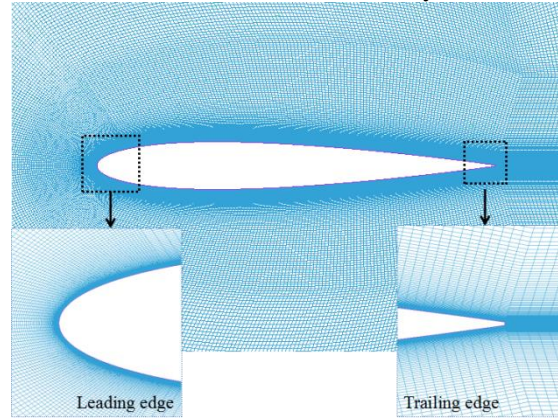where, k is the turbulent kinetic energy, ω is the specific turbulent dissipation, $\tilde{P}_k$ is defined as $\tilde{P}_k=\gamma_{eff}P_k$, $\tilde{D}_k$ is defined as $\tilde{D}_k=\min\left(\max\left(\gamma_{eff},0.1\right),1.0\right)D_k$, P_k and P_ω are production terms, D_k is the destruction term, F_1 is blending functions.

3. Numerical setup

As shown in figure 1(a), the computational domain and boundary conditions are set according to the experimental setup [12], containing two domains connected with a sliding grid interface. In which, the static domain has a length of 18c and a height of 6c, and the dynamic domain has a diameter of 4c. The interaction between the static domain and the dynamic domain is controlled by CFX expression language (CEL) subroutine. The velocity of the inlet and the pressure of outlet, and non-slip wall were adopted as boundary conditions. The inlet is sufficiently far (7 times chord length) from the airfoil to simulate an effectively unbounded flow field. Figure 1(b) show the boundary layer mesh and the refined grids around the foil, respectively. About 450 nodes were placed around the airfoil boundary layer, which is selected to meet $y^+=yu_\tau/v\approx1$, where y is the thickness of the first cell from the foil surface, and u_τ is the wall frictional velocity[20]. The 2D fluid mesh is composed of $2.2*10^5$ elements.

(a) Fluid domain and boundary conditions

(b) Fluid mesh details

Figure 1 2D fluid mesh and boundary conditions

In this study, the NACA0012 airfoil with a chord length of c=0.15m and a span of h=0.375m, is adopted, with a sinusoidal pitching motion, $\alpha=10+15\sin wt$, where α is the angle of attack (AOA), and w is the angular velocity, around an axis located at quarter of its chord from the leading edge, as shown in figure 2. The angular velocity w is obtained according to the reduced frequency K, which is defined as $wc/2U_\infty$. In this study, the reduced frequency K is setup as 0.05,0.1 and 0.2 respectively.

The mean free stream velocity U_∞ is 14m/s with turbulence intensity of 0.08%, which corresponds to a Reynolds number of $Re=1.35*10^5$ based on chord length of the airfoil.
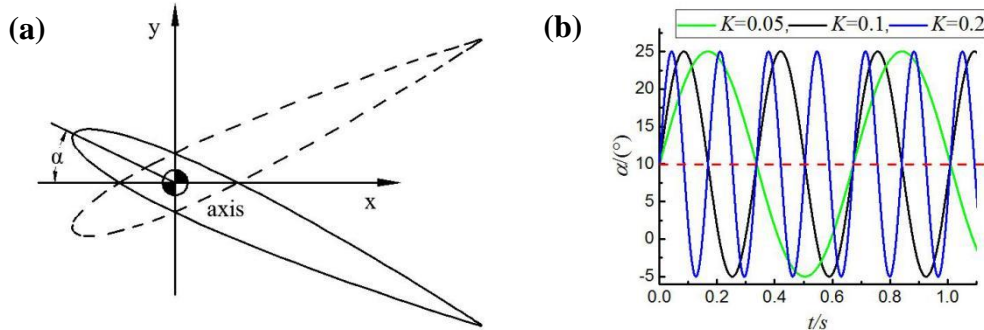

Figure 2 Pitching airfoil and motion feature

4. Results and discussion
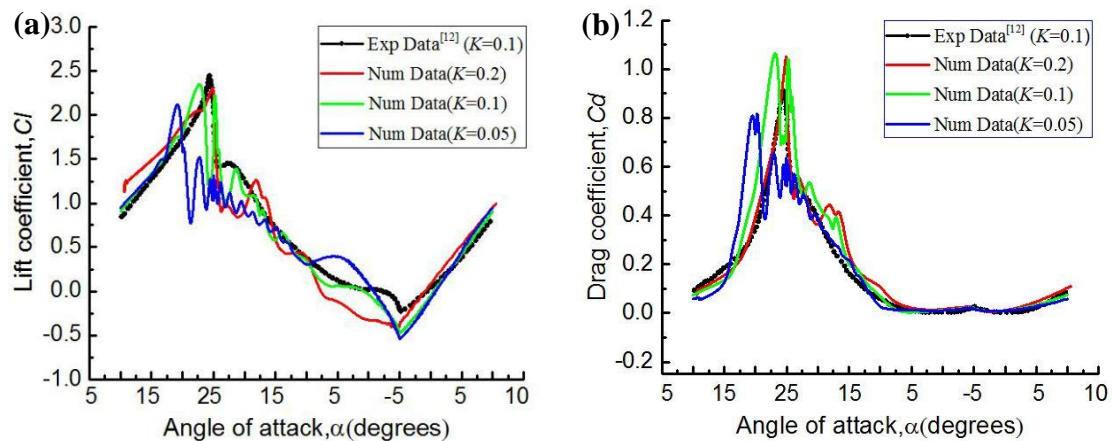
4.1. Numerical simulation validation

Figure 3 Comparison of the predicted lift (C_l) and drag (C_d) for transient flows with different reduced frequency (K=0.05, 0.1,0.2) for Re=135,000, U_∞=14m/s. (a) Lift coefficient. (b) Drag coefficient

The evolution of the lift coefficients C_l ($C_l = L/(0.5\rho U_\infty^2 sc)$) and drag coefficients C_d ($C_d = D/(0.5\rho U_\infty^2 sc)$) with the geometric angle of attack α for the sinusoidal pitching motion are presented in figure 3, where L and D are, respectively, the lift and drag. In Figure 3, the dynamic experimental results are obtained from Ref.[12]. It is shown that in the upstroke from $t_1(\alpha^+=-5°)$ to $t_7(\alpha^+=25°)$, the numerical results agree well with the experimental data, and the maximum of predicted lift coefficient C_l is very close to the measured value. In the down stroke, the predicted lift coefficients present a small amplitude and low-frequency oscillating behaviour from $t_7(\alpha^+=25°)$ to $t_{13}(\alpha^-=18.1°)$. This may due to the interaction between the induced secondary vortex on the leading and trailing edge, and the detailed analysis of the flow features is given in the following paragraphs.

To sum up, although the numerical results exist slightly discrepancies, two-dimensional studies by k-w SST model and the γ-Re_θ transition model are able to capture the mean features and qualitative tendencies of the dynamic stall phenomenon.

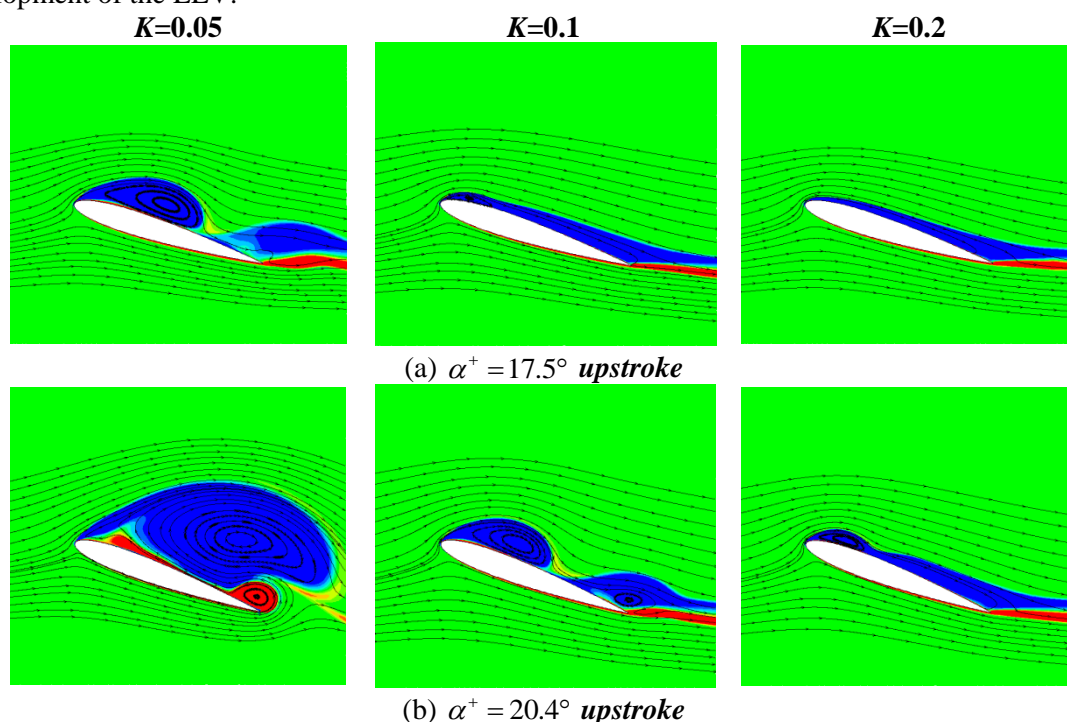### 4.2. Comparisons between K=0.05 and 0.1, 0.2

In section 4.1, the flow structures and the corresponding aerodynamic performance with the changes of angle of attack as K=0.1 are presented. From the mentioned detail above, the movement of airfoil

plays a important role in the flow structure. So in order to gain more insights of the flow structures during the dynamic stall, the flow structures at different reduced frequency emphasize to discuss in this section. The value of the reduced frequency is setup as 0.05, 0.1 and 0.2 respectively. For the sinusoidal pitching motion, the evolution of the transient flow structures and the corresponding aerodynamic responses with the changes of angle of attack can be divided into four phases: (i)attached flow, (ii) development of the Leading Edge Vortex (LEV), (iii) post-stall vortex shedding, and (iv) flow reattachment. In attached flow stage and flow reattachment stage, the effect of the reduced frequency is not obvious. So the analysis of the flow structures mainly focuses on development of the Leading Edge Vortex stage, post-stall vortex shedding.

4.2.1. Development of the Leading Edge Vortex stage. In figure 4, the contours of z-vorticity superimposed on the instantaneous streamlines in vortex developments stage for K=0.1 are presented. Meanwhile the contours of z-vorticity of K=0.05, 0.2 at the same angle of attack of K=0.1 are obtained and compared. It is prominent that the difference of the mechanism of the LEV development at different reduced frequency. Figure 5 shows comparisons of the predicted pressure coefficients at same geometric angles of attack for the different reduced frequency.

As K increased, the formation and rearward convection of the LEV was delayed to higher angles of attack, as shown in figure 4(a-c). At K=0.1, the formation and rearward convection of the LEV occurs at α^+ = 17.5 °. The LEV has covered the whole suction surface at α^+=23.5 °. As the development of the LEV, the max value of pressure coefficient moves the trailing edge in figure 5(a-c). When K=0.05, the LEV has covered two thirds of the suction surface at α^+ = 17.5 °. As the angle of attack reaches 20.4 °, the LEV has shed away. Compared to the case of K=0.1, the pressure coefficient is larger. At K=0.2, the formation of the LEV occurs at α^+ = 20.4 °. Compared to the case of K=0.1, the LEV only has covered the half suction surface at α^+=23.5 °. As shown in figure 5, the pressure coefficient is larger than the case of K=0.1.

Although the formation and rearward convection of the LEV was delayed with the increasing reduced frequency, the corresponding lift and drag coefficients all increased almost linearly with the increasing angle of attack α. Because the pressure coefficient become more and more larger with the development of the LEV.

K=0.05   **K=0.1**   **K=0.2**

(a) $\alpha^+ = 17.5°$ *upstroke*

(b) $\alpha^+ = 20.4°$ *upstroke*
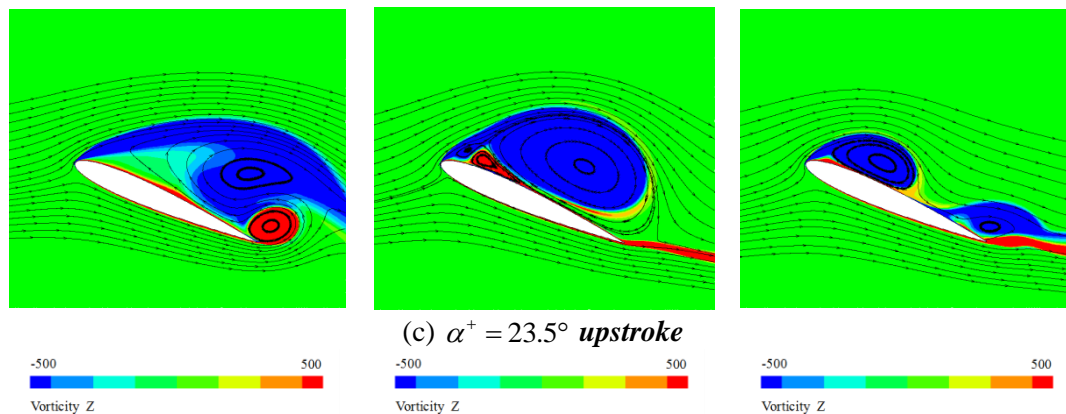
(c) $\alpha^+ = 23.5°$ *upstroke*

Figure 4 Contours of z-vorticity superimposed on the instantaneous streamlines in vortex developments stage at different reduced frequency (*K*=0.05,0.1,0.2)
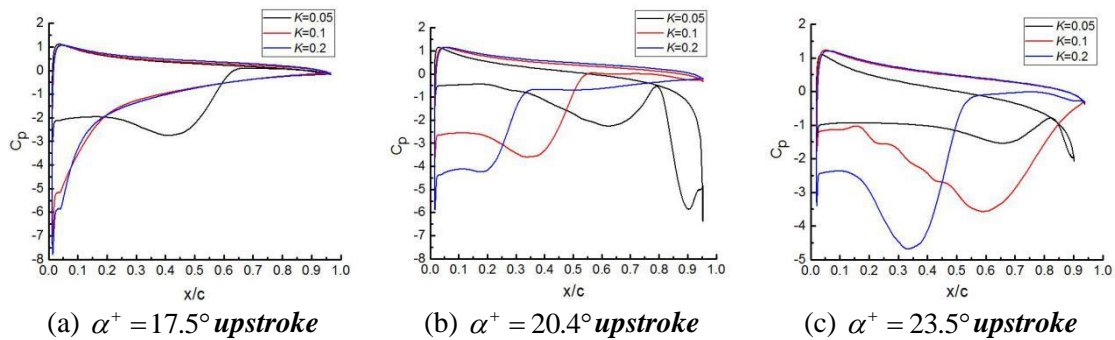

(a) $\alpha^+ = 17.5°$ *upstroke*   (b) $\alpha^+ = 20.4°$ *upstroke*   (c) $\alpha^+ = 23.5°$ *upstroke*

Figure 5 Comparisons of the predicted pressure coefficients at same geometric angles of attack for the different reduced frequency(*K*=0.05 ,0.1 and 0.2)

4.2.2. Post-stall vortex shedding stage. As shown in figure 6, the contours of z-vorticity superimposed on the instantaneous streamlines in post-stall vortex shedding stage at the same angle of attack for different reduced frequency are presented. It is find that the vortex-shedding phenomenon exists discrepancy at different reduced frequency. Comparisons of the predicted pressure coefficients at same geometric angles of attack for the different reduced frequency are shown in figure 7.

When *K*=0.1, it should be noted that at $\alpha^+ = 24.8°$ the LEV has shed away because of the interaction between the LEV and the TEV. Meanwhile the leading edge of the suction surface has induced a secondary vortex. In the downstroke phase at $\alpha^-=24.7°$, the secondary vortex has covered the whole suction surface, as shown in figure 4. With the development of the secondary vortex, the pressure coefficients become larger, as shown in figure 7(a-b). It should be noted that at $\alpha^-= 22.8°$ a new TEV rolls up, grows larger and squeezes the secondary vortex, while the secondary vortex begins to shed away, which is responsible for the reduction in the slope of the lift coefficient curve. As α increased, the multiple interaction between the LEV and the TEV results in small amplitude oscillating behavior in the lift and drag coefficient curves. When the angle of attack reaches to $\alpha^-=18.1°$, the flow begins to transit from turbulent to laminar.

When *K*=0.05, the vortex-shedding phenomenon was different from as *K*=0.1. At $\alpha^+ = 24.8°$ in upstroke phase, the LEV has shed away. As α increases, it is obvious observe that no secondary vortex was induced. Compared to the case of *K*=0.1, the pressure and lift coefficients are lower, as shown in figure 3 and figure 5. Increasingly, when *K*=0.2, the vortex-shedding phenomenon was different of the cases of *K*=0.05, 0.1. At $\alpha^- = 24.7°$ in downstroke phase, the LEV has shed away and the secondary vortex has spanned over approximately one third of the suction surface, while the trailing edge vortex is induced. Compared to the case of *K*=0.1, the secondary vortex begins to shed away at $\alpha^- = 22.8°$.

The secondary vortex cannot covers the whole suction surface because the oscillating velocity is too fast to develop the secondary vortex. Meanwhile, the fluctuations of the pressure and lift coefficients are more obvious.
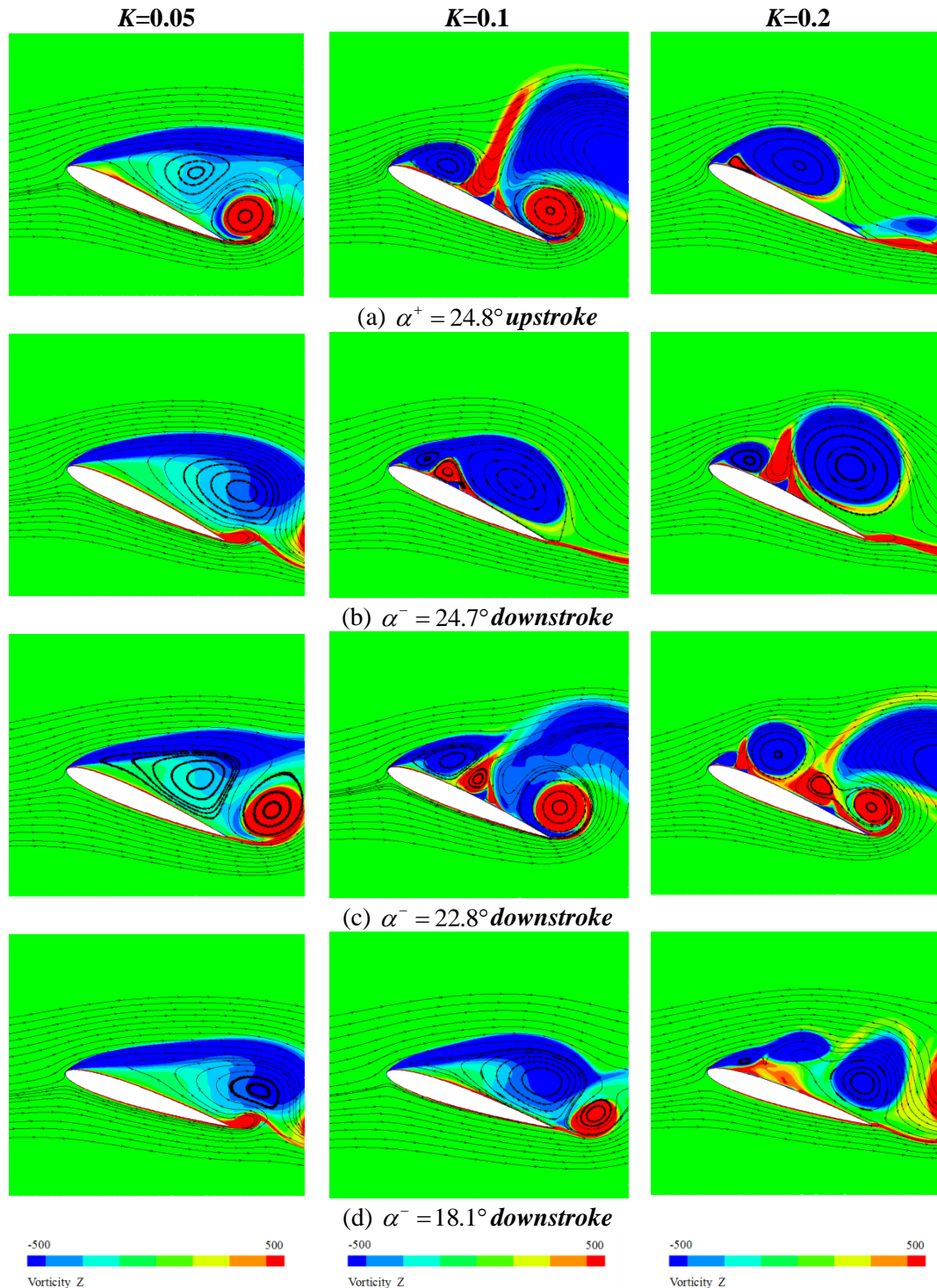

Figure 6 Contours of z-vorticity superimposed on the instantaneous streamlines in Post-stall vortex shedding stage at different reduced frequency(K=0.05,0.1,0.2)
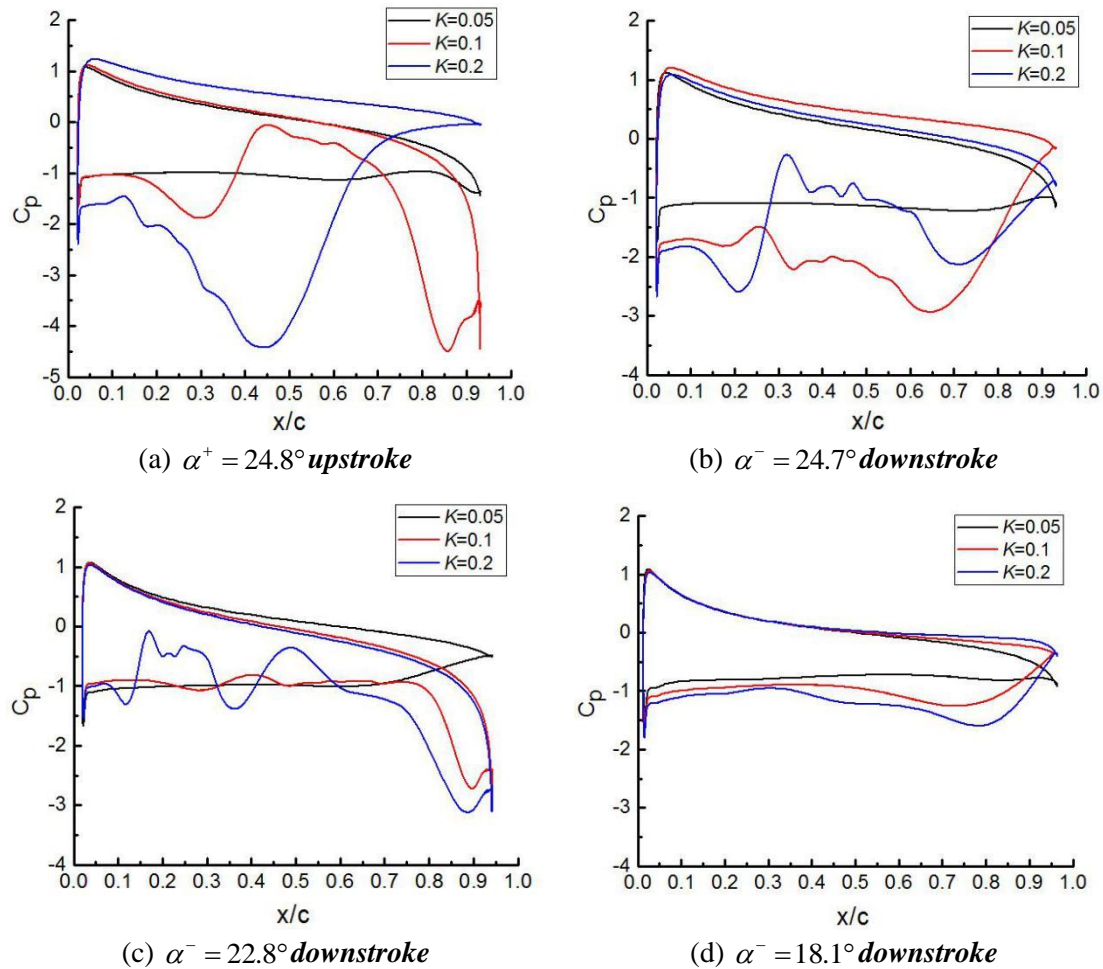
(a) $\alpha^+ = 24.8°\,upstroke$ (b) $\alpha^- = 24.7°\,downstroke$

(c) $\alpha^- = 22.8°\,downstroke$ (d) $\alpha^- = 18.1°\,downstroke$

Figure 7 Comparisons of the predicted pressure coefficients at same geometric angles of attack for the different reduced frequency(K=0.05 ,0.1 and 0.2)

5. Conclusion

In this study, the k-ω SST turbulence model with γ-Re_θ transition model has been used to simulate the dynamic stall phenomenon for a sinusoidal pitching NACA0012 airfoil. Contrast to the experimental results, the numerical results have been validated carefully. The influence of the reduced frequency on the flow evolution and dynamic performance is enormous at development of the Leading Edge Vortex stage, post-stall vortex shedding. The main conclusions are as following:

During the development of the Leading Edge Vortex stage, the increasing reduced frequency could delay dynamic stall to a higher angle, even delay in the downstroke.

During post-stall vortex shedding stage, the mechanism of post-stall vortex shedding present different style at different reduced frequency. When K=0.1, the secondary vortex forms and covers the whole suction face again along with the shedding of LEV. Compared to the case of K=0.1, no secondary vortex was induced for K=0.05. However, When K=0.2, the secondary vortex cannot cover the whole suction surface again because the oscillating velocity is too fast to develop the secondary vortex.

References
[1]   Melício R, Mendes V M F, Catalão J P S. 2011 Transient analysis of variable-speed wind turbines at wind speed disturbances and a pitch control malfunction. *Applied Energy*. 88(4):1322-1330.

[2]   González L G, Figueres E, Garcerá G, et al. 2010 Maximum-power-point tracking with reduced mechanical stress applied to wind-energy-conversion-systems. *Applied Energy*. 87(7):2304-2312.

[3]   Karbasian H R, Esfahani J A, Barati E. 2016 The power extraction by flapping foil hydrokinetic turbine in swing arm mode. *Renewable Energy*. 88:130-142.

[4]   Lei H, Zhou D, Lu J, et al. 2017 The impact of pitch motion of a platform on the aerodynamic performance of a floating vertical axis wind turbine. *Energy*. 119:369-383.

[5]   Mckenna R, Leye P O V D, Fichtner W. 2016 Key challenges and prospects for large wind turbines. *Renewable & Sustainable Energy Reviews*. 53:1212-1221.

[6]   Lu K, Xie Y, Zhang D, et al. 2015 Systematic investigation of the flow evolution and energy extraction performance of a flapping-airfoil power generator. *Energy*. 89:138-147.

[7]   Huang B, Wu Q, Wang GY. 2014 Numerical simulation of unsteady cavitating flows around a transient pitching hydrofoil. *Sci China Tech Sci*. 57(1): 101-116.

[8]   Wu Q, Huang B, Wang GY, Gao Y.2015 Experimental and numerical investigation of hydroelastic response of a flexible hydrofoil in cavitating flow. *International Journal of Multiphase Flow*. 74: 19-33.

[9]   Wang GY, Wu Q, Huang B. 2017 Dynamics of cavitation-structure interaction. *Acta Mechanica Sinica*. 33(4): 685-708.

[10]   Yang J, Peng C, Xiao J, et al. 2012 Application of videometric technique to deformation measurement for large-scale composite wind turbine blade. *Applied Energy*. 98(1):292-300.

[11]   Mckinney W, Delaurier J. 2012 Wingmill: An Oscillating-Wing Windmill. *Journal of Energy*. 1(2):80-87.

[12]   Lee T, Gerontakos P. 2004 Investigation of flow over an oscillating airfoil. *Journal of Fluid Mechanics*. 512: 313–341

[13]   Liu X, Lu C, Liang S, et al. 2017 Vibration-induced aerodynamic loads on large horizontal axis wind turbine blades . *Applied Energy*.

[14]   Danao L A, Qin N, Howell R. 2012 A numerical study of blade thickness and camber effects on vertical axis wind turbines. *Proceedings of the Institution of Mechanical Engineers Part A Journal of Power & Energy*. 226(7):867-881.

[15]   Huang B, Ducoin A, Young LY. 2013 Physical and numerical investigation of cavitating flows around a pitching hydrofoil. *Phys Fluids*. 25(10): 2109.

[16]   Wu Q, Huang B, Wang GY. 2016 Lagrangian-Based Investigation of the Transient Flow Structures around a Pitching Hydrofoil. *Acta Mechanica Sinica*. 32(1): 64-74.

[17]   Bhat S S, Govardhan R N. 2013 Stall flutter of NACA0012 airfoil at low Reynolds numbers. *Journal of Fluids & Structures*. 41:166-174.

[18]   Lai J C S, Platzer M F. 2015 Jet Characteristics of a Plunging Airfoil. *Aiaa Journal*. 37(12):1529-1537.

[19]   Gharali K, Johnson D A. 2013 Dynamic stall simulation of a pitching airfoil under unsteady free stream velocity. *Journal of Fluids & Structures*. 42(4):228-244.

[20]   Menter FR. 1992 Improved two-equation k-ω turbulence models for aerodynamic flows. *NASA Tech*. Memorandu 34, 103975.

[21]   Langtry RB, Menter FR, Likki SR, et al. 2006 A correlation-based transition model using local

variables-Part I: model formulation. *J. Turbomachinery*. 128: 413-422.

[22] Menter FR, Langtry RB, Likki SR, et al. 2006 A correlation-based transition model using local variables-Part II: test cases and industrial applications. *J. Turbomachinery*. 128: 423-434.

[23] Menter FR, Langtry RB, Völker S. 2006. Transition modeling for general purpose CFD codes. *Flow Turbulence Combust*. 77(1): 277-303.